Supplementary materials for

Metastable interphase induced pre-strain compensation enables efficient and stable perovskite solar cells

Hongyu Xu *et al.*

Experimental Section

Materials

Lead iodide (PbI_2, 99.99%), and cyclohexanemethylamine hydroiodide (CHMAI, 99.9%) were purchased from Tokyo Chemical Industry Co., Ltd (TCI, Japan). Formamidinium iodide (FAI, >99.99%) was purchased from Greatcell Solar Materials Pty Ltd (Australia). $FAPbI_3$ crystals were obtained by the method we reported previously (*Nat. Energy 2024, DOI: 10.1038/s41560-024-01642-3*). 2,2',7,7'-Tetrakis(*N*,*N*-di-p-methoxyphenyl-amine)-9,9'-spirobifluorene (Spiro-OMeTAD, 99.9%) was purchased from Borun Chemical (China). Methylammounium chloride (MACl, 99.9%), [6,6]-phenyl-C61-butyric acid methyl ester ($PC_{61}BM$, 99.9%), 2,9-dimethyl-4,7-diphenyl-1,10-phenanthroline (BCP, 99.5%) and fluorine-doped tin oxide (FTO) glass (sheet resistance of 7 Ω sq^{-1}) were purchased from Advanced Election Technology Co., Ltd (China). The lithium bis(trifluoromethylsulfonyl)imide salt (LiTFSI, 99.95% trace metals basis), 4-tert-butylpyridine (tBP, 96%), $SnCl_2{\cdot}2H_2O$ (>99.995%), urea (99%), thioglycolic acid (TGA, 98%), and lead chloride ($PbCl_2$, 99.999%) were purchased from Sigma-Aldrich (USA). *N*,*N*-dimethylformamide (DMF, 99.8%), dimethyl sulfoxide (DMSO, 99.7%), chlorobenzene (CB, 99.8%), isopropanol (IPA, 99.5%), ethanol (EtOH, 99.5%), acetonitrile (ACN, 99.9%), and ethyl acetate (EA, 99.9%) were purchased from Acros Organics (USA). Acetone (HPLC), deionized (DI) water, hydrochloric acid (HCl, 37 wt.% in water) and isopropanol (IPA, HPLC) were purchased from Sinopharm Chemical Reagent Co., Ltd (China). All reagents were used as received without further purification.

The Solutions Preparation

The perovskite precursor solution of $FAPbI_3$ was obtained by dissolving 1.8 M $FAPbI_3$ crystals and 0.63 M MACl into the mixed solvent of DMF:DMSO: (v:v = 860:140). The solution of $PbCl_2$ was prepared by dissolving 5 mg $PbCl_2$ into 10 mL DI water, stirred overnight at 30 °C. The solution was diluted to 0.25 mg/mL with DI water before use. The solution of hole transporting layer (HTL) was prepared by dissolving 72.3 mg spiro-OMeTAD, 28.8 μL tBP, 17.5 μL LiTFSI (520 mg/mL in ACN) in 1 mL CB. The chemical bath deposition (CBD) solution for SnO_2 was prepared by mixing urea (625 mg), HCl (625 μL), TGA (12.5 μL), and $SnCl_2{\cdot}2H_2O$ (137.5 mg) into DI water (50 mL), where DI water needs to be oxygenated for 4 hours before use. The post-treatment solution was prepared by dissolving CHMAI in IPA (6 mg/mL).

Device Fabrication

The FTO glass substrate was cleaned by sonication in cleaning liquid, DI water, acetone, and IPA for 10 minutes each. One edge of the FTO substrate was taped with a kapton tape to prevent deposition of SnO_2. The FTO substrates were soaked into the CBD solution in a glass reaction vessel and reacted at 90 °C for 4 hours. After the reaction is complete, the FTO/SnO_2 substrate was removed from the reaction vessel and cleaned via sonication with DI water and IPA for 5 minutes each. Then, The FTO/SnO_2 substrate was annealed in an ambient environment with a relative humidity (RH) of ~30% at 170 °C for 60 minutes. For the $PbCl_2$-modified FTO/SnO_2 substrates, the $PbCl_2$ solution was spin-coated on the substrates by a one-step program at 3,000 rpm for 30 seconds. Then, the substrates were annealed at 100 °C for 15 minutes in ambient air with a RH of ~30%. The perovskite precursor solution was deposited onto the substrates by a consecutive two-step program at 2,000 rpm for 10 seconds with a ramping rate of 200 rpm/s, and 5,000 rpm for 20 seconds with a ramping rate of 2,000 rpm/s. During the second step, 120 μL EA was poured onto the substrate before 5 seconds to the end. Then, the samples were annealed at 150 °C for 10 minutes in the air with a RH of 25~35%. Next, the samples were transferred onto a hotplate of 100 °C inside glovebox with nitrogen for 10 minutes. The post-treatment solution was deposited on the perovskite layer at 6,000 rpm for 30 seconds. Then the films were heated at 100 °C for 5 minutes. Further, the HTL solution was spin-coated on the perovskite layer at 4,000 rpm for 20 seconds. A 80-nm thick Au electrode was thermally evaporated onto the samples in the vacuum chamber ($<4\times10^{-4}$ Pa) with a deposition rate of 0.1-1.0 Å/s.

Characterizations

The current density-voltage (*J-V*) characteristics were measured with a 2400 Series Source Meter (Keithley Instruments, USA) under AM 1.5G illumination using a 150 W Class AAA solar simulator (XES-40S1, SAN-EI). The light intensity of 100 mW/cm^2 was calibrated using a standard monocrystalline silicon solar cell with a KG-5 filter. The active area of the device was defined with an aperture area of 0.07066 cm^2. The sweeping conditions are: reverse scan (1.22 V to -0.02 V, scan rate 10 mV/s, delay time 20 milliseconds) and forward scan (-0.02 V to 1.22 V, scan rate 10 mV/s, delay time 20 milliseconds). The external quantum efficiency (EQE) spectrum was measured using an EQE system (QE-R 3011, Enli) at DC mode. The perovskite films were investigated by grazing incidence wide angle X-ray scattering, the wavelength of X-ray was 1.2398Å (GIWAXS, BL 17B1 beamline of the Shanghai Synchrotron Radiation Facility (SSRF)), scanning electron microscopy (SEM, FEI Nova Nano SEM 430, FEI, USA). Time-of-flight secondary ion mass spectrometry results were obtained from a 50 μm × 50 μm area on the sample surface. The ejected secondary ions were accelerated by a sample bias of 3.0 kV, so the secondary ions could gain enough kinetic energy to reach the SIMS detector. All the secondary-ion data presented in the profiles were normalized by total ion intensities (TOF-SIMS, Model TOF-SIMS V, ION-TOF GmbH). Temperature-dependent photoluminescence (PL) was conducted under continuous weak-light excitation using a xenon

lamp coupled with a monochromator (FLS1000, Edinburgh Instruments, UK). Time-resolved photoluminescence (TRPL) of the perovskite films was measured using time-correlated single photon counting (TCSPC) following excitation by a 398 nm picosecond pulsed diode laser at a repetition rate of 250 and 62.5 KHz (PicoHarp, LDH-D-C-405M). The resultant PL was collected and coupled into a grating spectrometer (Princeton Instruments, SP-2558), which directed the spectrally dispersed PL onto a photon-counting detector (PDM series from MPD), whose timing was controlled with a PicoHarp300 TCSPC event timer. Optical-Pump Terahertz-Probe (OPTP) Spectroscopy: An amplified laser system (Spectra Physics, MaiTai-Ascend-Spitfire), with a 5 kHz repetition rate, centre wavelength of 800 nm and pulse duration of 35 fs was used to generate the THz radiation using a spintronic emitter. The THz probe was then focused onto the sample, overlaid with a 400 nm excitation pump that was generated using a Beta Barium Borate (BBO) crystal. The THz radiation transmitted through the sample was then detected via free-space electro-optical sampling in a ZnTe (110) crystal of thickness 200 μm. SCLC measurement was conducted based on electron-only devices with the architecture of FTO/SnO_2/Perovskite/PC_{61}BM/BCP/Ag.

Supplementary Note 1

According to the Braggs law, Hooke's law and equations of equilibrium, the residual stress (σ) of perovskite lattices can be obtained as follows,

$$\sigma = \frac{E}{(1+\upsilon)sin^2\chi}\left(\frac{d_\chi - d_0}{d_0}\right) \quad (1)$$

where E is Young's modulus and υ is Poisson's ratio of the perovskite film, respectively. E and υ are evaluated as 10 GPa and 0.3, respectively. χ is the scattering vector angle, pertaining to the perovskite film surface normal direction. d_0 is the interplanar spacing of the strain-free perovskite corresponding to a given crystal plane.

Due to strain $\varepsilon_\chi = \frac{d_\chi - d_0}{d_0}$, we further convert Equation 1 to Equation 2 as follow:

$$\varepsilon_\chi = \sigma\frac{(1+\upsilon)}{E}sin^2\chi \quad (2)$$

By fitting the ε_χ as a function of $sin^2\chi$, the residual stress can be calculated from the above formula.

According to the Bragg's Law and generalized Hooke's Law, the $2\theta - \sin^2\psi$ also can be given as follows,

$$\sigma = -\frac{E}{2(1+\nu)}\frac{\pi}{180}\cot\theta_0\frac{\partial(2\theta)}{\partial\sin^2\psi} \quad (3)$$

where θ_0 is half of the scattering angle $2\theta_0$, corresponding to a given diffraction peak for strain-free perovskite, 2θ is the scattering angle for the actual perovskite, ψ is the angle, the diffraction vector N_k with respect to the normal of the sample surface. By fitting the $2\theta - \sin^2\psi$ relationship, we can obtain the residual stress through the above formula.

Supplementary Note 2

We fit a stretched exponential function as follows to the PL intensity to account for the local distribution of monoexponential decay rates:

$$I = I_0 e^{(\frac{t}{\tau_{char}})^\beta} \quad (1)$$

Effective lifetime is given by:

$$\tau_{eff} = \frac{\tau_{char}}{\beta}\Gamma(\frac{1}{\beta}) \quad (2)$$

where τ_{char} is the characteristic lifetime corresponding to the time taken for the PL intensity to drop to I_0/e, and β is the distribution coefficient that encompasses the case for monoexponential decays for the case $\beta = 1$, and the cases for a range of decay times (or potentially higher-order effects) as it decreases.

To account for the PL originating from electron-hole recombination, we further double the effective fitted lifetime in order to extract the monomolecular charge-carrier recombination rate k_1 as follows,

$$k_1 = \frac{1}{2\tau_{eff}} \tag{3}$$

assuming $I \propto k_2 n^2$ at our excitation fluences of 75, 150, and 510 nJ/cm^2.

Supplementary Note 3

Charge-carrier sum mobility

Time-resolved variations in the THz transmission ($\Delta T/T$) through the sample can be measured by varying the time delay between the pump and probe beams, and this change in electric-field transmission at the peak of the THz pulse (t_{gate}) can be in turn related to the change in the photoconductivity (ΔS) of the thin film (whose thickness *d* is much smaller than the THz wavelengths λ_{THz}), using

$$\Delta S = -\epsilon_0 c(n_a + n_b)\frac{\Delta T(t_{gate} = 0)}{T} \tag{1}$$

where $\epsilon_0 c$ is the invert of the vacuum impedence, and n_a and n_b are the refractive indices of the mediums surrounding the sample (vacuum and the substrate).

The charge-carrier mobility (μ) and change in photoconductivity (ΔS) have a linear relationship that holds for low fluences (< 50 μJ/cm^2), described using

$$\mu = \frac{\Delta S A_{eff}}{Ne} \tag{2}$$

where A_{eff} is the effective area of overlap between the optical pump and the THz probe, and *N* is the number of photoexcited charge carriers.

The number of photoexcited charge carriers can be calculated using

$$N = \Phi\frac{E\lambda}{hc}(1 - R_{pump} - T_{pump}) \tag{3}$$

where Φ is the branching ratio of free charge-carriers to photons absorbed, $(1 - R_{pump} - T_{pump})$ is the fraction of the 400 nm pump beam absorbed by the sample, λ and *E* are the wavelength and pulse energy of the excitation pulse, and $\frac{E\lambda}{hc} = N_{ph}$ is the number of photons in a pump pulse.

We can then combine Equation 1, Equation 2, and Equation 3 to calculate the effective charge-carrier mobility as follows,

$$\Phi\mu = -\epsilon_0 c(n_a + n_b)\frac{A_{eff}hc}{Ee\lambda(1 - R_{pump} - T_{pump})}\left(\frac{\Delta T(t_{gate}, t_{pump-probe} = 0)}{T}\right) \quad (4)$$

This effective mobility is the effective sum mobility of photogenerated electrons and holes, and it reflects the true sum mobility when the photons absorbed are fully converted to free charge carriers ($\Phi = 1$).

Transient decay fitting

The ΔS transients can be globally fitted to extract k_2, with k_1 and k_3 either ignored (set to 0) or set to a reasonable value, as the excitation fluences used for the experiments conducted here lead the fluence-dependent decays over the first nanosecond after excitation to be primarily affected by bimolecular electron-hole recombination captured by the rate constant k_2. Charge-carrier dynamics in perovskite semiconductors can be generally described using

$$\frac{dn}{dt} = -k_1 n - k_2 n^2 - k_3 n^3 \quad (5)$$

where *n* is the photogenerated charge-carrier density, *t* is the time following the excitation pulse, k_1 is the first-order monomolecular recombination rate related to non-radiative trap-mediated recombination, k_2 is the second-order bimolecular recombination rate related to radiative band-to-band recombination, and k_3 represents the Auger recombination rate involving three carriers. Here, trap-mediated recombination rates are too low to have any influence over the first nanosecond (hence k_1 may be ignored), while charge-carrier densities were kept below the limit for which Auger recombination begins to dominate (k_3 may be ignored).

This leads to the analytical expression for *n*:

$$n(t) = \frac{1}{(\frac{1}{n_0} + k_2 t)} \tag{6}$$

where n_0 is the initial number density of free charge carriers at $t = 0$.

Using Equation 2 and Equation 4, the photogenerated charge-carrier density is proportional to the change in the photoconductivity (ΔS):

$$n = \Phi\, C\, \Delta S(t) \tag{7}$$

where C = $\tilde{n}/\Delta S_0$ is the proportionality constant between the initial change in photoconductivity (ΔS_0) and absorbed photon density ($\tilde{n}$), given by:

$$\tilde{n} = \frac{E\lambda}{hcdA_{eff}}(1 - R_{pump} - T_{pump}) \tag{8}$$

Substituting Equation 8 into Equation 5 gives:

$$\frac{d(\Delta S)}{dt} = -\Phi k_2 C\, (\Delta S)^2 \tag{9}$$

The global fits across all fluences to this ODE are used to extract the effective bimolecular recombination rate constant Φk_2. Similar to the calculated mobilities, the values presented for k_2 are underestimates for the true intrinsic values.

To account for the spatially-varying charge-carrier density across the thickness of the film, the fitting algorithm considers an exponentially decaying charge-carrier density; done by dividing the film into 30 equally-thick slabs and individually computing the decay function for each slab.

Finally, the diffusion length L_D can then be calculated by using the diffusion coefficient *D* (calculated from the mobility) and recombination rate R_n (calculated from the recombination rates k_1, k_2, and k_3):

$$L_D = \sqrt{\frac{D}{R_n}} = \sqrt{\frac{k_B T \mu}{e(k_1 + k_2 n + k_3 n^2)}} \tag{10}$$

where *T* is the temperature, and k_B is the Boltzmann constant, and *n* is the charge-carrier density photogenerated under normal operating conditions (1 sun) equalling roughly to $1 \times 10^{15}\ cm^{-3}$, for which k_2 and k_3 make only small contributions.

Supplementary Note 4

We calculate the exciton binding energy from the temperature-dependent PL results to reflect the excitonic feature of the charge carriers. According to the Arrhenius equation, we are able to gain the exciton binding energy by fitting the relationship between the integrated PL intensities (area of PL peak) and temperatures.

$$I = \frac{I_0}{1 + Ae^{-E_b/k_B T}} \quad (1)$$

where I is the integrated PL intensity, I_0 is the integrated PL intensity at 0 K, E_b is the activation energy, k_B is the Boltzmann constant, A is a fitting constant, respectively.

Supplementary Note 5

The predominant electron-phonon coupling mechanism in metal halide perovskites is attributed to Fröhlich interaction between the longitudinal optical (LO) mode phonons and electrons. In this case, the dependence of the full width at half-maximum (FWHM) of the PL spectra on temperature $\Gamma(T)$ can be described by the independent Boson model:

$$\Gamma(T) = \Gamma_0 + \Gamma_{LO} = \Gamma_0 + \frac{\gamma_{LO}}{e^{E_{LO}/k_B T} - 1} \quad (1)$$

where Γ_0 is the temperature-independent term induced by disorder and imperfections. Γ_{LO} stands for the contribution from LO phonons, and γ_{LO} is the coupling strength between electrons and LO phonons, E_{LO} is the representative energy of LO phonons described by Bose-Einstein distribution function, k_B is the Boltzmann constant.

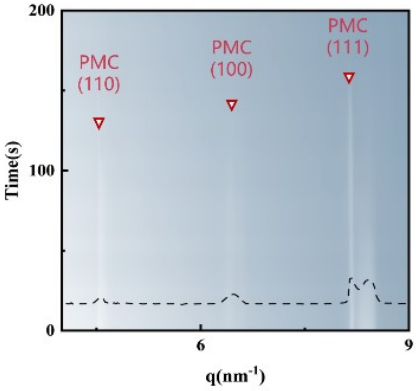

Supplementary Figure 1. A partial enlargement of Fig. 1c. The red triangle indicates the PMC phase.

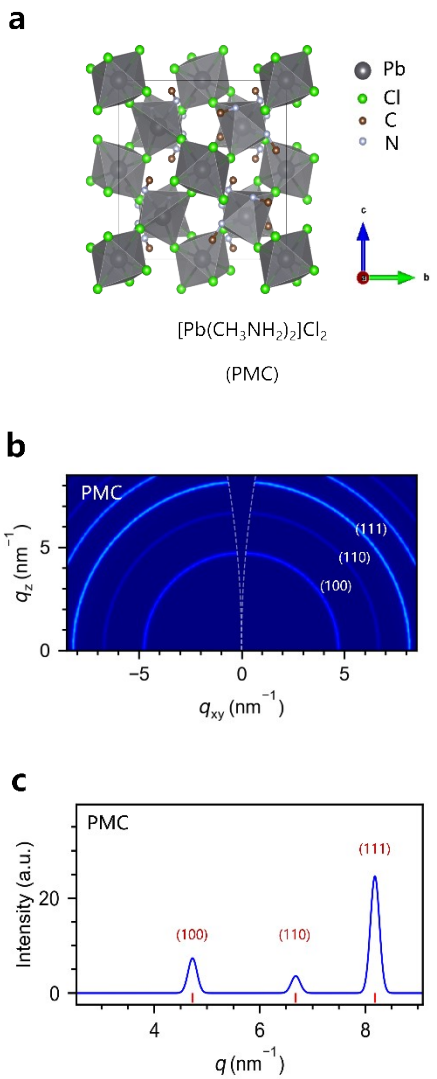

Supplementary Figure 2. (a) The crystal structure of the PMC phase. (b) The simulated 2D GIWAXS image of the PMC phase. (c) The simulated 1D GIWAXS profile of the PMC phase.

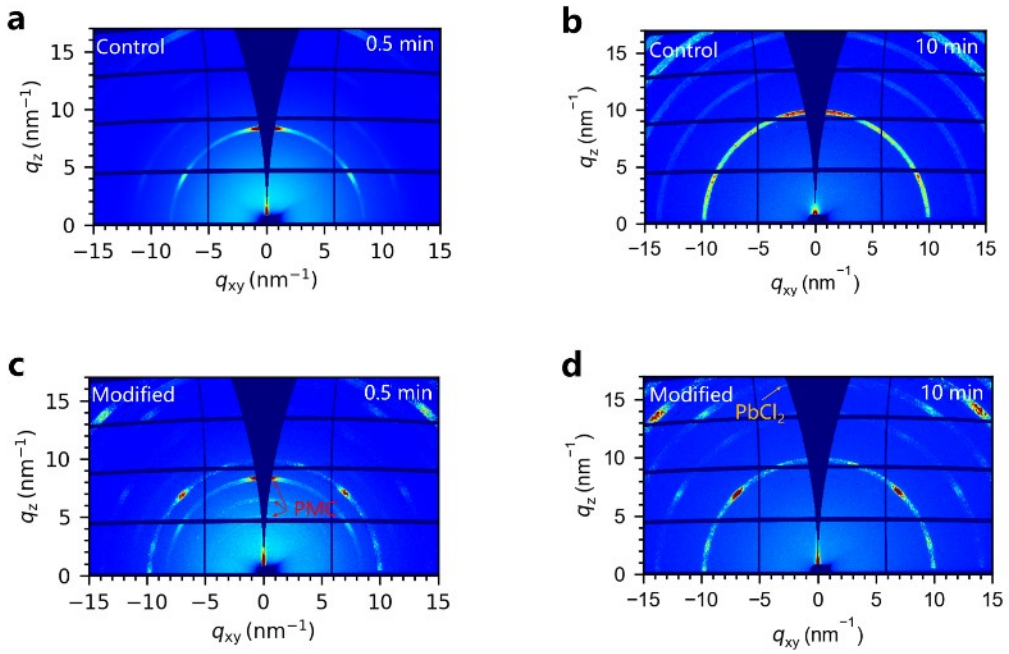

Supplementary Figure 3. 2D GIWAXS images of the control and modified perovskite films at different annealing times. The red arrows indicate the PMC phase, and the orange arrow indicates the $PbCl_2$ phase.

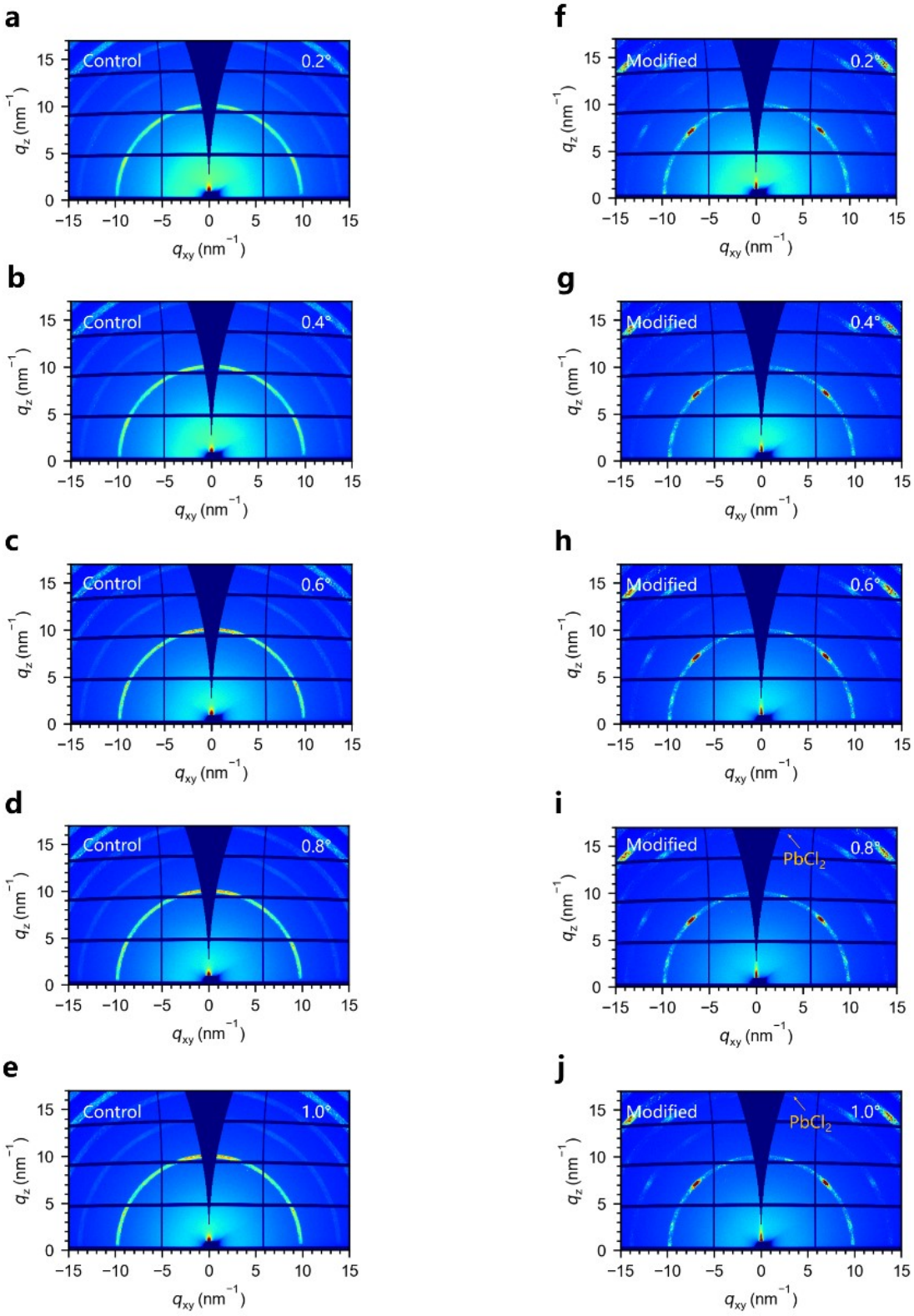

Supplementary Figure 4. 2D GIWAXS images of the control and modified perovskite films at different incidence angles. The orange arrow indicates the $PbCl_2$ phase.

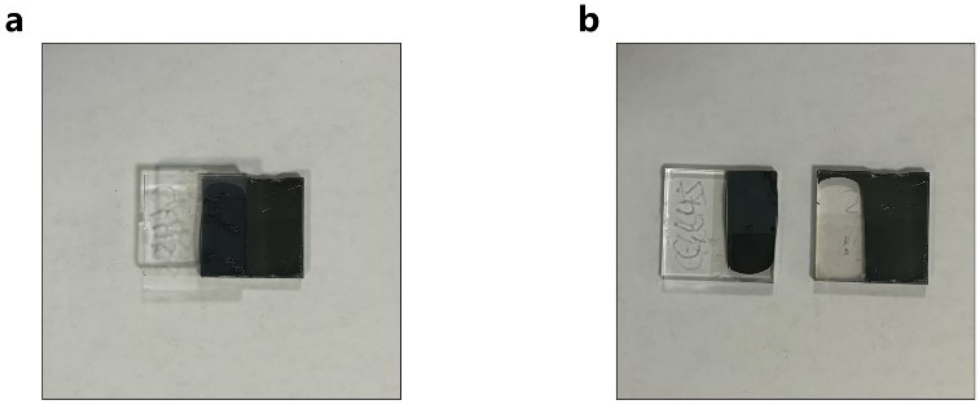

Supplementary Figure 5. The perovskite film was peeled off from the substrate using UV-curing glue. In order to make the UV-curing glue and the perovskite surface adhere tightly and improve the success rate of peeling, the perovskite surface can be rinsed with IPA solution in advance and left to stand overnight after the glue is cured.

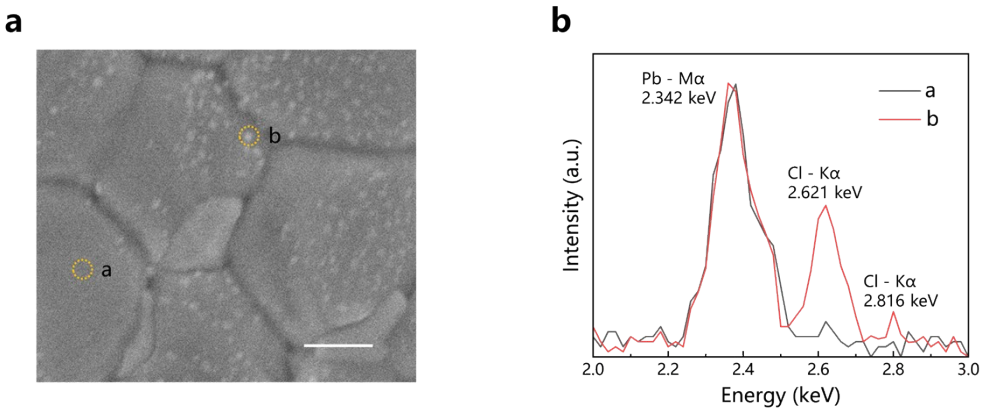

Supplementary Figure 6. (a) The top-view SEM image from the bottom of the modified perovskite film. Scale bar, 400 nm. (b) The energy dispersive X-ray spectrometry (EDX) spectra of Region a and Region b in (a).

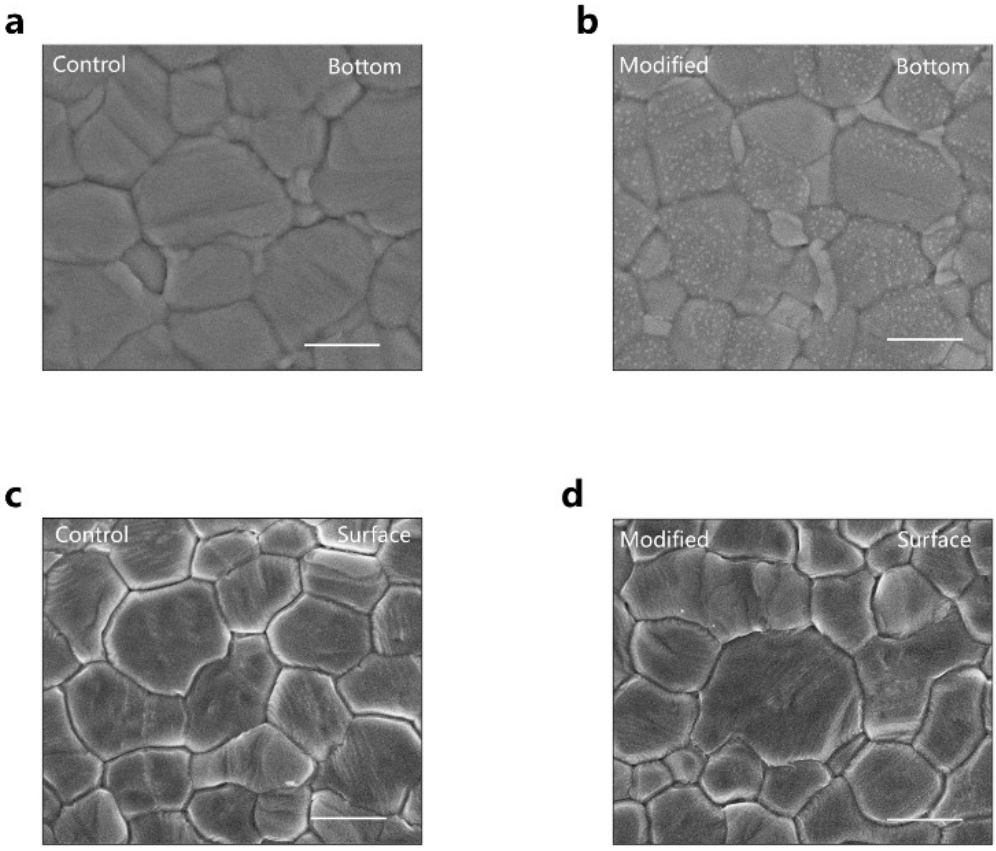

Supplementary Figure 7. Top-view SEM images of the bottom and surface of different perovskite films. Scale bars, 1 μm.

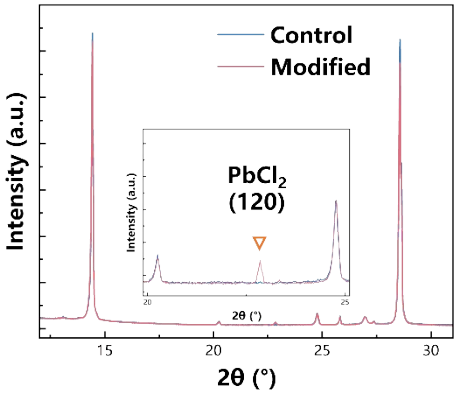

Supplementary Figure 8. XRD patterns of the control and modified perovskite films. The orange triangle indicates the $PbCl_2$ phase.

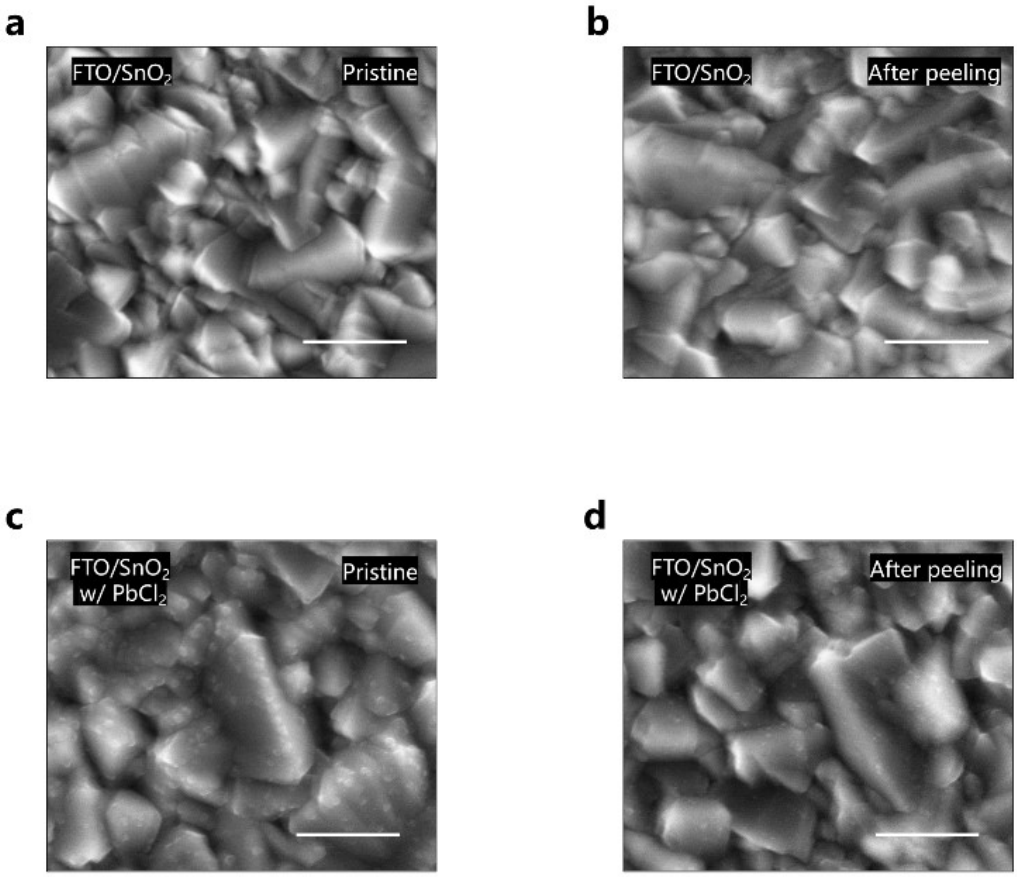

Supplementary Figure 9. Top-view SEM images of the pristine substrates (a,c) and the substrates after peeling off the perovskite films (b,d). Scale bars, 400 nm.

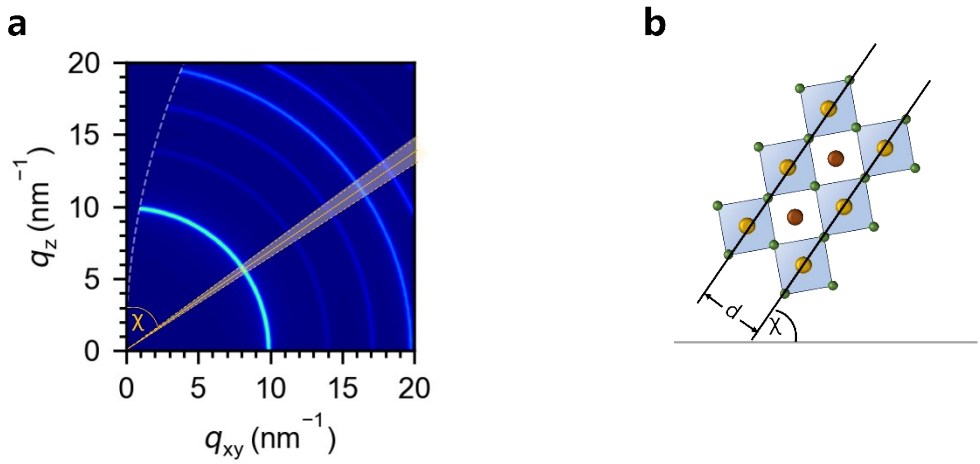

Supplementary Figure 10. (a) Integrating the fan-shaped area around angle χ. (b) The relationship between the χ angle and the crystal plane orientation.

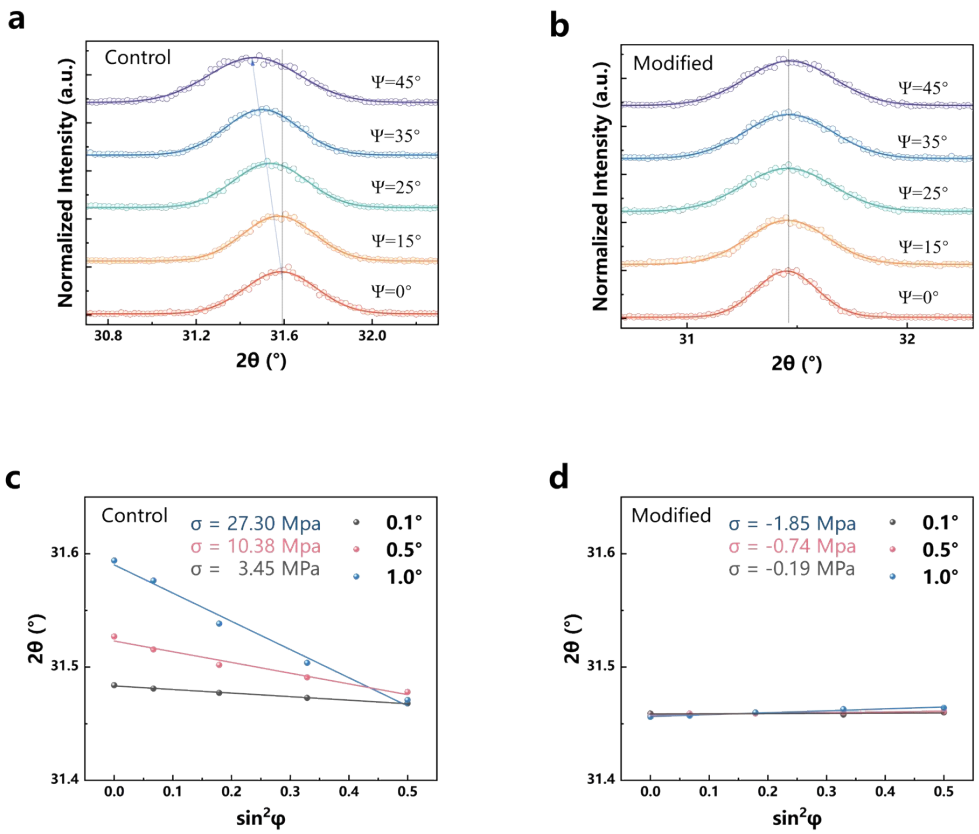

Supplementary Figure 11. (a,b) Variation in 2θ of (210) plane for Control (a) and Modified (b) films at different φ angles. The grazing incidence angle is 1°. (c,d) The relationship between 2θ and $\sin^2\varphi$ of (210) plane for Control (c) and Modified (d) films at different grazing incidence angles.

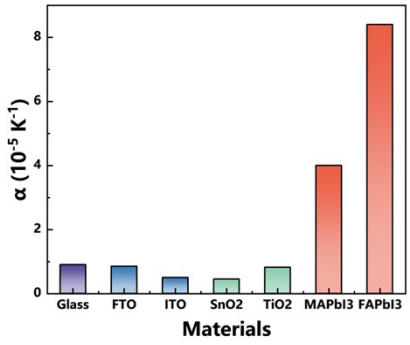

Supplementary Figure 12. Thermal expansion coefficients (TECs, α) of different substrate materials and perovskites.

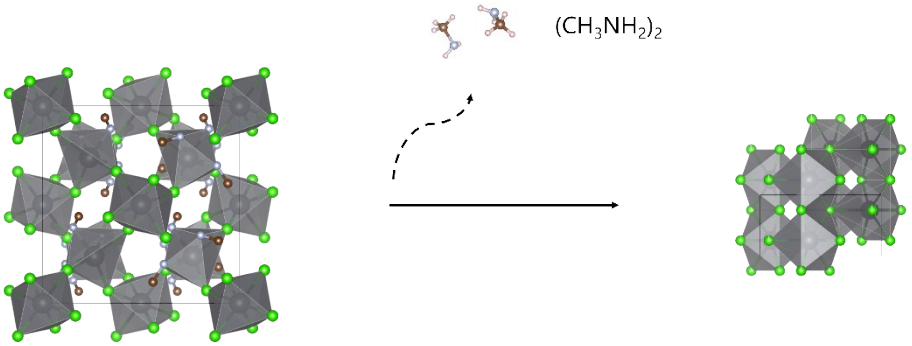

Supplementary Figure 13. The schematic diagram of the transformation from PMC phase to $PbCl_2$ phase.

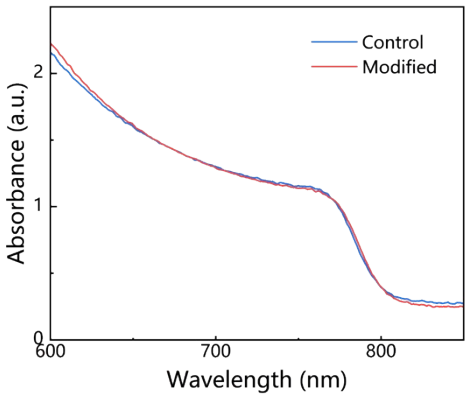

Supplementary Figure 14. UV-vis absorption spectra of the control and modified perovskite films at room temperature.

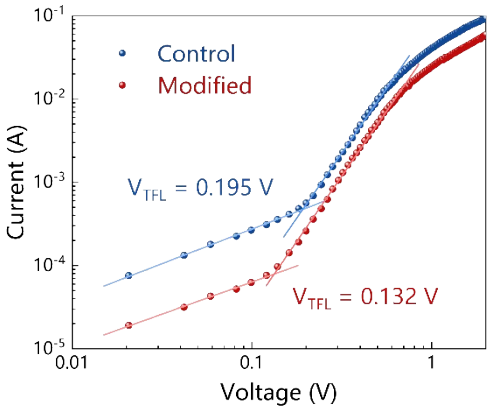

Supplementary Figure 15. Space-charge-limited current (SCLC) results of different electron-only devices based on control and modified perovskite films.

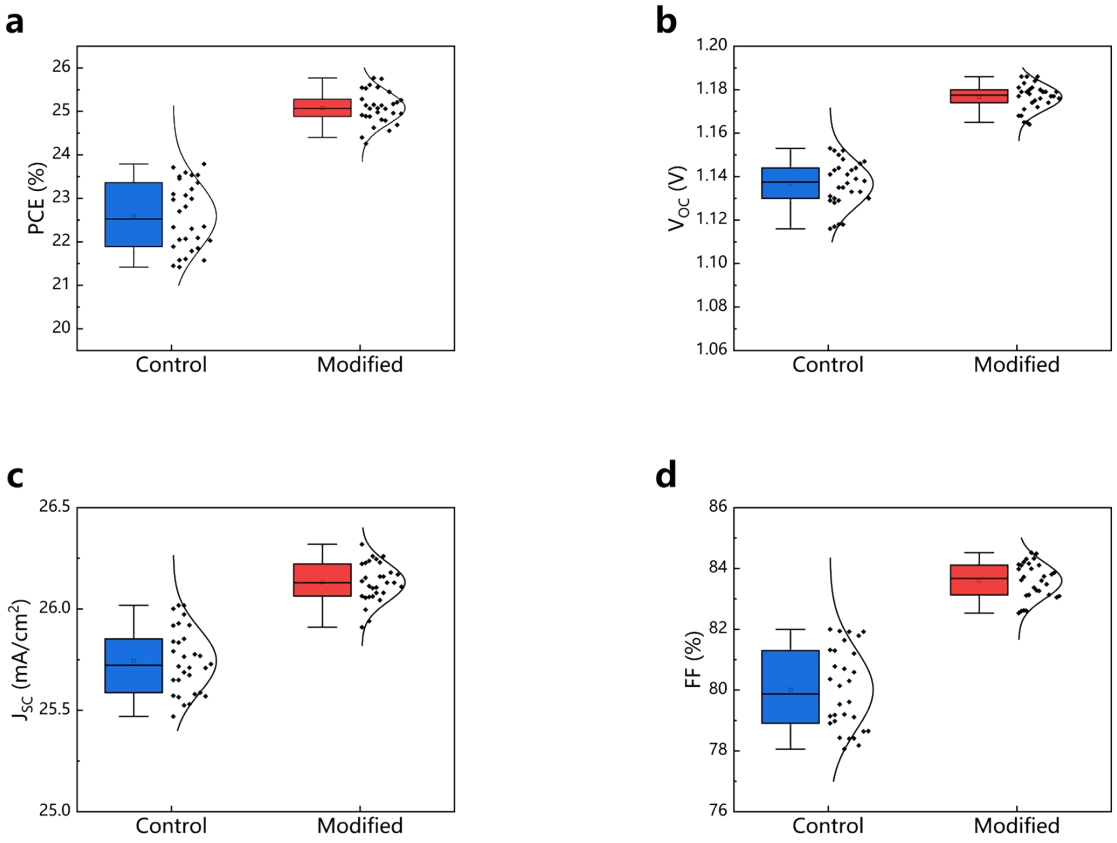

Supplementary Figure 16. Statistical data on the photovoltaic performance of the control and modified PSC devices.

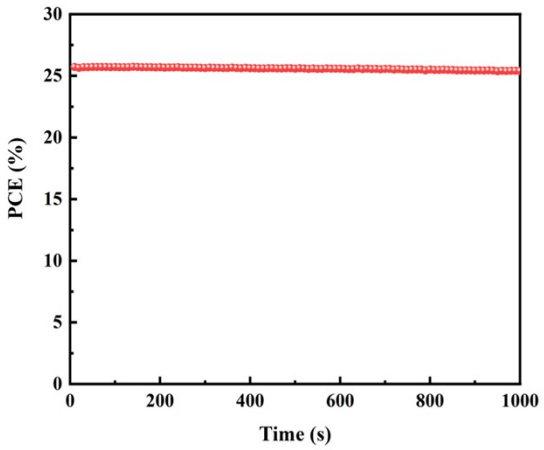

Supplementary Figure 17. The stable power output at the maximum power point of a modified PSC device.

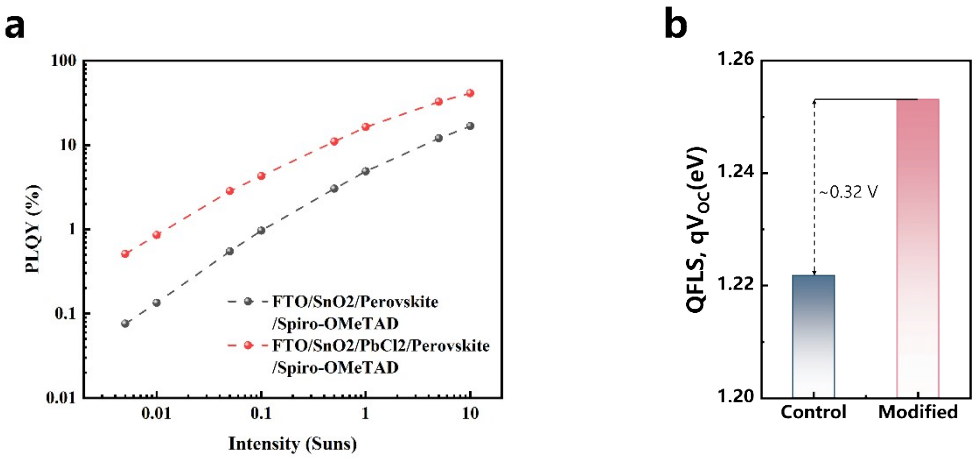

Supplementary Figure 18. (a) Light intensity dependence of PLQY for different PSCs. (b) The calculated quasi-Fermi level splitting (QFLS) for different PSCs.

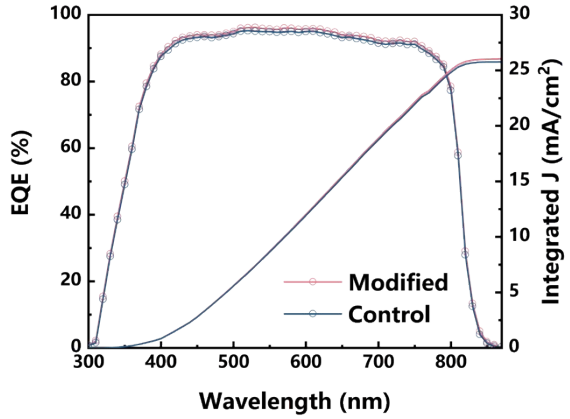

Supplementary Figure 19. The external quantum efficiency (EQE) results of different PSCs.

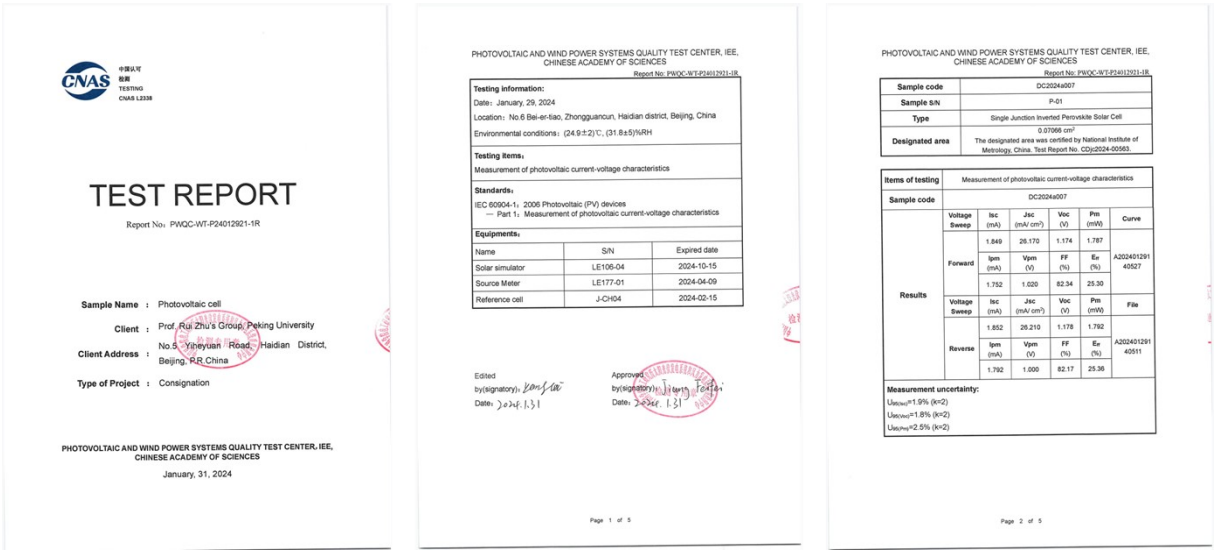

CNAS 中国认可 检测 TESTING CNAS L2338

TEST REPORT

Report No：PWQC-WT-P24012921-1R

Sample Name ： Photovoltaic cell

Client ： Prof. Rui Zhu's Group, Peking University

Client Address ： No.5 Yiheyuan Road, Haidian District, Beijing, P.R.China

Type of Project ： Consignation

PHOTOVOLTAIC AND WIND POWER SYSTEMS QUALITY TEST CENTER, IEE, CHINESE ACADEMY OF SCIENCES

January, 31, 2024

PHOTOVOLTAIC AND WIND POWER SYSTEMS QUALITY TEST CENTER, IEE, CHINESE ACADEMY OF SCIENCES

Report No: PWQC-WT-P24012921-1R

Testing information:

Date：January, 29, 2024

Location：No.6 Bei-er-tiao, Zhongguancun, Haidian district, Beijing, China

Environmental conditions：(24.9±2)℃, (31.8±5)%RH

Testing items：

Measurement of photovoltaic current-voltage characteristics

Standards：

IEC 60904-1：2006 Photovoltaic (PV) devices
— Part 1：Measurement of photovoltaic current-voltage characteristics

Equipments：

Name	S/N	Expired date
Solar simulator	LE106-04	2024-10-15
Source Meter	LE177-01	2024-04-09
Reference cell	J-CH04	2024-02-15

Edited by(signatory)：

Date：2024.1.31

Approved by(signatory)：

Date：2024.1.31

Page 1 of 5

PHOTOVOLTAIC AND WIND POWER SYSTEMS QUALITY TEST CENTER, IEE, CHINESE ACADEMY OF SCIENCES

Report No: PWQC-WT-P24012921-1R

Sample code	DC2024a007
Sample S/N	P-01
Type	Single Junction Inverted Perovskite Solar Cell
Designated area	0.07066 cm² The designated area was certified by National Institute of Metrology, China. Test Report No. CDJz2024-00563.

Items of testing	Measurement of photovoltaic current-voltage characteristics					
Sample code	DC2024a007					
Results	Voltage Sweep	Isc (mA)	Jsc (mA/cm²)	Voc (V)	Pm (mW)	Curve
	Forward	1.849	26.170	1.174	1.787	A202401291 40527
		Ipm (mA)	Vpm (V)	FF (%)	Eff (%)	
		1.752	1.020	82.34	25.30	
	Voltage Sweep	Isc (mA)	Jsc (mA/cm²)	Voc (V)	Pm (mW)	File
	Reverse	1.852	26.210	1.178	1.792	A202401291 40511
		Ipm (mA)	Vpm (V)	FF (%)	Eff (%)	
		1.792	1.000	82.17	25.36	

Measurement uncertainty:

$U_{Rel(Isc)}$=1.9% (k=2)

$U_{Rel(Voc)}$=1.8% (k=2)

$U_{Rel(Pm)}$=2.5% (k=2)

Page 2 of 5

Supplementary Figure 20. Certification reports from the Photovoltaic and Wind Power Systems Quality Test Center, IEE, Chinese Academy of Sciences. The certified reverse-scanning PCE for the modified PSC is 25.36% and the forward-scanning PCE is 25.30%, respectively.

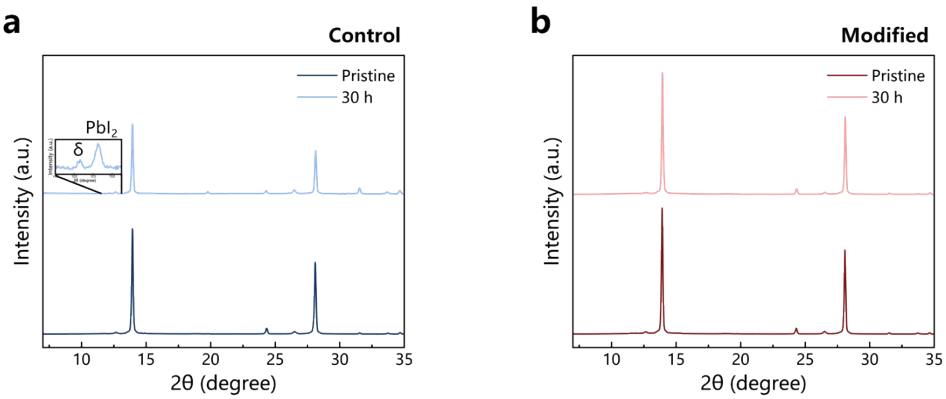

Supplementary Figure 21. XRD patterns of (a) the control perovskite film and (b) modified perovskite film. Stability variations of unencapsulated perovskite films upon heating at 65 °C in nitrogen atmosphere.

Supplementary Table 1. Unit cell volumes of PMC phase and $PbCl_2$ phase.

Chemical formula	$3\{[Pb(CH_3NH_2)_2]Cl_2\}$	$3(PbCl_2)$
Volume ($Å^3$)	2351.9	937.1

Supplementary Table 2. The parameters for the carrier dynamics of different perovskite films.

Stack	Mobility $\Phi\mu$ ($cm^2V^{-1}s^{-1}$)	PL lifetime τ (μs)	TRPL - k_1 ($10^6\ s^{-1}$)	OPTP - k_2 ($10^{-11}\ cm^3s^{-1}$)	Diffusion length L_D (μm)
Control	43.9	0.216	2.30	9.7	6.8
Modified	49.0	0.686	0.73	9.7	12.2

Supplementary Table 3. Fitting parameters of different perovskite films in Fig. 3h.

	Γ_0 (meV)	γ_{LO} (meV)	E_{LO} (meV)	R^2
Control	31.7±0.5	159.4±11.4	31.1±1.3	0.998
Modified	24.4±0.4	89.6±4.5	21.2±0.8	0.999

Supplementary Table 4. Photovoltaic parameters of PSCs in Fig. 4b.

Device		V_{OC} (V)	J_{SC} (mA/cm^2)	FF (%)	PCE (%)
Modified	Forward	1.182	26.12	83.4	25.75
	Reverse	1.182	26.14	83.6	25.83
Control	Forward	1.132	25.73	78.5	22.86
	Reverse	1.153	25.90	80.1	23.92

Supplementary Table 5. Photovoltaic parameters of PSCs in Fig. 4c.

Area	Device	V_{OC} (V)	J_{SC} (mA/cm^2)	FF (%)	PCE (%)
1.05 cm^2 (with mask)	Modified	1.178	26.03	79.0	24.22
	Control	1.148	25.57	75.5	22.16

Supplementary Table 6. The initial PCEs of the PSCs referred to Fig. 4d.

Sample	PCE (%)
Control-1	23.62
Control-2	23.12
Control-3	23.75
Control-4	23.44
Control-5	23.39
Control-6	23.60
Control-7	23.31
Control-8	23.87
Modified-1	25.17
Modified-2	25.37
Modified-3	25.81
Modified-4	24.96
Modified-5	25.65
Modified-6	25.08
Modified-7	25.79
Modified-8	25.55

Supplementary Table 7. The initial PCEs of the PSCs referred to Fig. 4e.

Sample	PCE (%)
Control-1	22.95
Control-2	23.76
Control-3	23.70
Control-4	23.31
Control-5	23.52
Control-6	23.34
Control-7	23.87
Control-8	23.09
Modified-1	25.69
Modified-2	25.39
Modified-3	25.65
Modified-4	25.11
Modified-5	25.23
Modified-6	25.04
Modified-7	25.52
Modified-8	25.48

Supplementary Table 8. The initial PCEs of the PSCs referred to Fig. 4g.

Sample	PCE (%)
Control-1	22.87
Control-2	23.60
Control-3	23.25
Control-4	23.79
Control-5	23.84
Control-6	23.75
Control-7	23.38
Control-8	23.02
Modified-1	25.04
Modified-2	25.68
Modified-3	25.12
Modified-4	25.70
Modified-5	25.43
Modified-6	25.75
Modified-7	25.82
Modified-8	25.15